minerals

MDPI

Article

Petrogenesis and Tectonic Implications of the Granite Porphyry in the Sinongduo Ag-Pb-Zn Deposit, Central Tibet: Constraints from Geochronology, Geochemistry, and Sr-Nd Isotopes

Peng Zhang [1,2], Zhuang Li [3,4,*], Feng Zhao [3] and Xinkai Liu [3]

1 College of Earth and Planetary Sciences, Chengdu University of Technology, Chengdu 610059, China
2 Sichuan Institute of Land Science and Technology, Chengdu 610074, China
3 School of Geography and Resource Science, Neijiang Normal University, Neijiang 641100, China
4 Key Laboratory of Continental Dynamics, Northwest University, Xi'an 710069, China
* Correspondence: lizhuang@njtc.edu.cn

Abstract: The Paleocene ore deposits related to the India–Asia continental collision are widely distributed in the Gangdese metallogenic belt. Among these, Sinongduo is the first discovered epithermal Ag-Pb-Zn deposit in the Lhasa terrane. However, there is still controversy over the ore-forming magma in this deposit. This study mainly reports new zircon U-Pb isotopic ages, whole-rock geochemistry, and Sr-Nd isotopic data for the granite porphyry from the Sinongduo deposit, aiming to discuss the petrogenesis and tectonic setting of the granite porphyry and its genetic link between the Ag-Pb-Zn mineralization. The results show that zircon U-Pb analyses yield ages of 62.9 ± 0.5 Ma and 59.0 ± 0.7 Ma for the granite porphyry, indicating that it formed during the Paleocene period. The timing of the granite porphyry intrusion is contemporaneous with the mineralization, suggesting that it is most likely the ore-forming magma in the Sinongduo deposit. The granite porphyry has high SiO_2 and K_2O, moderate Al_2O_3, and low Na_2O, CaO, and FeO^T contents, and it displays significant enrichments in LREEs and LILEs and depletions in HREEs and HFSEs, with negative Eu anomaly. The granite porphyry is a peraluminous series and can be classified as S-type granite. Moreover, the granite porphyry shows relatively high ratios of $(^{87}Sr/^{86}Sr)_i$ and low values of $\varepsilon_{Nd}(t)$. The geochemical and isotopic compositions of the granite porphyry from the Sinongduo area are similar to those of the upper continental crust, which suggests that the granite porphyry was most likely derived from the melting of the upper continental crust in the Lhasa terrane during the India–Asia collisional tectonic setting.

Keywords: granite porphyry; petrogenesis; tectonic setting; Paleocene; Sinongduo; Gangdese

check for updates

Citation: Zhang, P.; Li, Z.; Zhao, F.; Liu, X. Petrogenesis and Tectonic Implications of the Granite Porphyry in the Sinongduo Ag-Pb-Zn Deposit, Central Tibet: Constraints from Geochronology, Geochemistry, and Sr-Nd Isotopes. *Minerals* **2024**, *14*, 710. https://doi.org/10.3390/min14070710

Academic Editors: Yitian Wang, Changqing Zhang and Giorgio Garuti

Received: 11 June 2024
Revised: 5 July 2024
Accepted: 10 July 2024
Published: 12 July 2024

Copyright: © 2024 by the authors. Licensee MDPI, Basel, Switzerland. This article is an open access article distributed under the terms and conditions of the Creative Commons Attribution (CC BY) license (https://creativecommons.org/licenses/by/4.0/).

1. Introduction

The evolution of the Neo-Tethys and the India–Asia collision led to the formation of the Himalaya–Tibetan Orogen, which is considered a prominent tectonic event in Earth's history [1–4]. The Lhasa terrane, an important region in the Tibetan Plateau, underwent complex subduction processes during the evolution of the Neo-Tethys and the subsequent India–Asia collision [5–7]. This region now showcases extensive volcanic formations such as the Linzizong volcanic successions and Gangdese batholith, located north of the Yarlung Zangbo suture zone [8]. These volcanic formations, dating between 65 and 40 million years ago, represent the magmatic response to the India–Asia continental collision and play a significant role in the geological makeup of the Lhasa terrane [9,10]. In addition to the Cenozoic porphyry Cu-Mo deposits found within the Gangdese metallogenic belt (GMB), a variety of other mineral deposits, like skarn-type, hydrothermal-type, and cryptoexplosive breccia-type Ag-Pb-Zn deposits, have been identified in the Lhasa terrane [11–15].

The Sinongduo deposit, located in central Tibet within the Linzizong volcanic successions of the GMB, is known as the first discovered epithermal Ag-Pb-Zn deposit. Its formal

recognition occurred in 2010 following an extensive five-year survey and exploration effort, revealing Pb + Zn reserves exceeding 350,000 tons and Ag reserves surpassing 400 tons. The average grades of these ores are approximately 5% for Pb + Zn and 50 g/t for Ag. Previous studies on Sinongduo primarily emphasized its geological characteristics, mineral composition, alteration zone, geochronology, and source of ore-forming metals [16–24]. However, the ore-forming magma in this deposit has always been unclear. In this paper, we present new zircon U-Pb ages, major and trace elements, and Sr-Nd isotopic compositions for the granite porphyry, aiming to determine the timing of the magmatism and its link with the Ag-Pb-Zn mineralization at the Sinongduo deposit. Moreover, these results will refine our knowledge of the petrogenesis and tectonic setting of the granite porphyry in the Lhasa terrane.

2. Geological Background

The Tibetan Plateau (Figure 1a) is divided into the Qiangtang terrane, the Lhasa terrane, and the Himalayas from north to south, with the Jinsha (JSSZ), Longmu Tso-Shuanghu (LSSZ), Bangong-Nujiang (BNSZ), and Yarlung Zangbo (YZSZ) suture zones separating them (Figure 1b; [7,25]). The Lhasa terrane can be further classified into northern, central, and southern subterranes based on differences in basement rock and sedimentary cover (Figure 1b,c; [25]). The central Lhasa subterrane is mostly covered by Mesozoic and Cenozoic sedimentary units, along with dispersed Mesozoic–Cenozoic volcanic sedimentary rocks [6,25–27]. These sedimentary units contain collision-related granitoids from the Paleocene–Eocene period, as well as subduction-related arc granitoids from the Late Triassic to Cretaceous period [28,29]. The volcanic–sedimentary rocks in the region consist of lower Cretaceous Zenong and Duoni formations [30,31], as well as Paleocene–Eocene Linzizong volcanic rocks [8,32]. The Linzizong volcanic successions erupted mainly from 69 to 43 Ma and are comprised of calc-alkaline andesitic flows, tuffs and breccias, and dacitic to rhyolitic ignimbrites [8,33]. Based on the duration of magmatic activity, these volcanic successions are subdivided into the lower Dianzhong (69–60 Ma), middle Nianbo (56–54 Ma), and upper Pana (52–43 Ma) formations [34–36]. Previous research has primarily focused on the Linzizong volcanic successions near Lhasa city [37,38] and the Linzhou basin [32,39]. Dianzhong volcanism is typically associated with late oceanic subduction and initial continental collision, while the Nianbo and Pana volcanic events are linked to the collision [36,40]. In addition to this, granitic rocks are prevalent in the Tibetan Plateau, including the extensive plutonic belt known as the Gangdese batholith [41,42]. Research shows that the Gangdese batholith was active from the Late Triassic to the Miocene period, experiencing three magmatic peaks during the Late Jurassic (ca. 170–150 Ma) [43], Early Cretaceous (ca. 125–100 Ma) [44], and Paleocene–Eocene [45–47] epochs. The lithologies found in the Gangdese batholith consist of granodiorite, diorite, granite porphyry, and monzogranite, commonly containing hornblende or biotite [47], with the majority being I-type granitoids [41,48,49].

The Gangdese porphyry copper belt (GPCB) is located in the southern Lhasa subterrane and has been the subject of extensive exploration and research [50,51]. There are three main mineralization phases identified in the area. The first phase, occurring between 180 and 160 Ma, is related to Neo-Tethys subduction and is associated with the Xiongcun porphyry Cu-Au deposit [52,53]. The second phase, occurring during 65–40 Ma, is related to the India–Asia collision and includes the Tangbula and Sharang porphyry Mo deposits [54], as well as the Mengya'a skarn Pb-Zn deposits [11]. The third phase, occurring between 20 and 10 Ma, is related to the post-collision between India and Asia and includes several porphyry-skarn mineralization events, such as the Jiama, Qulong, Bangpu, Chongjiang, Tinggong, Zhunuo, and Jiru Cu-Mo deposits [55–58]. In addition to the GPCB, there is also a distinct Ag-Pb-Zn metallogenic belt that runs parallel to it. This belt mainly consists of skarn and hydrothermal type Ag-Pb-Zn deposits, including cryptoexplosive breccia and epithermal deposits. The skarn type deposits in this belt include the Longmala, Lietinggang, and Leqingla deposits [59,60], while the hydrothermal Ag-Pb-Zn deposits mainly

include the Narusongduo and Sinongduo deposits, which are predominantly found in the Linzizong volcanic rocks [21,61].

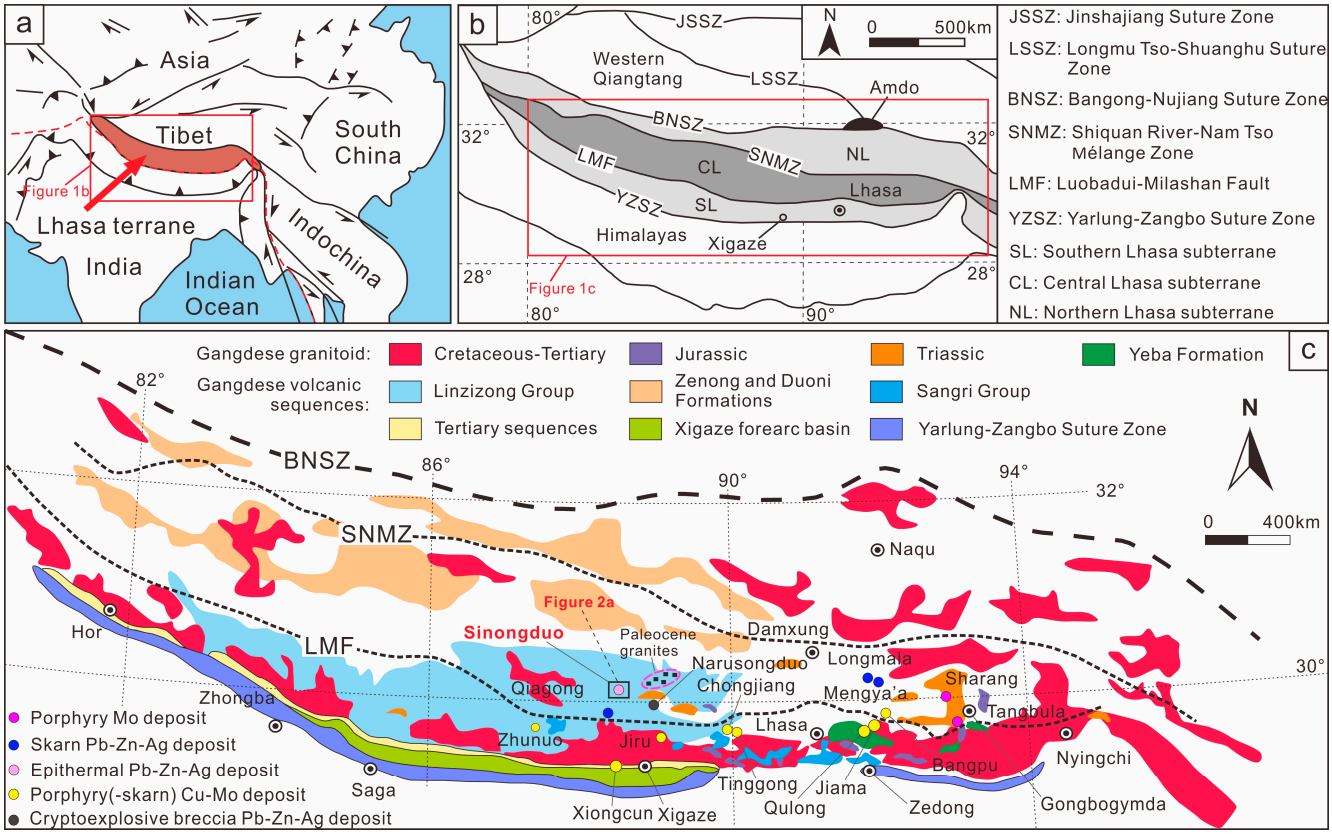


Figure 1. (**a**) Simplified map showing the location of the Himalayan–Tibetan orogeny; (**b**) tectonic framework of the Lhasa terrane (modified after [7]); (**c**) diagram showing the distribution of the magmatic rocks and the associated deposits in the Lhasa terrane (modified after [52]).

3. Deposit Geology

The Sinongduo deposit, situated in the southern margin of the central Lhasa subterrane about 170 km west of Xigaze (Figure 1c), encompasses three distinct orebodies: a hydrothermal vein-type Ag-Pb-Zn, a cryptoexplosive breccia-type Pb-Zn-Ag, and independent silver orebodies. The mineralization mainly occurred between 63.1 and 60.9 Ma based on the sericite Ar-Ar isotopic dating [21]. The Linzizong volcanic succession is prominently displayed throughout the Sinongduo district, which mainly comprise the rhyolite porphyry, crystal tuff, volcanic breccia, and dacite (Figure 2a). In this deposit, the ore-bearing wall rocks comprise rhyolite porphyry, crystal tuff, and volcanic breccia, while the intrusive rocks mainly consist of SE-trending granite porphyry and biotite granite porphyry. The exposed area of granite porphyry batholith is about 0.3 square kilometers, and granite porphyry, biotite granite porphyry, and rhyolite porphyry are in close spatial contact (Figure 2a). The granite porphyry at the Sinongduo deposit is intruded by the biotite granite porphyry vein, with the rhyolite porphyry overlying it.

The ore structures mainly consist of typical brecciated (Figure 3a) and veined structures (Figure 3b) formed by hydrothermal filling metasomasis, with a few banded and disseminated structures. The ore textures are mainly featured by hydrothermal metasomatism and crystallization, followed by textures formed by solid solution separation and pressure.

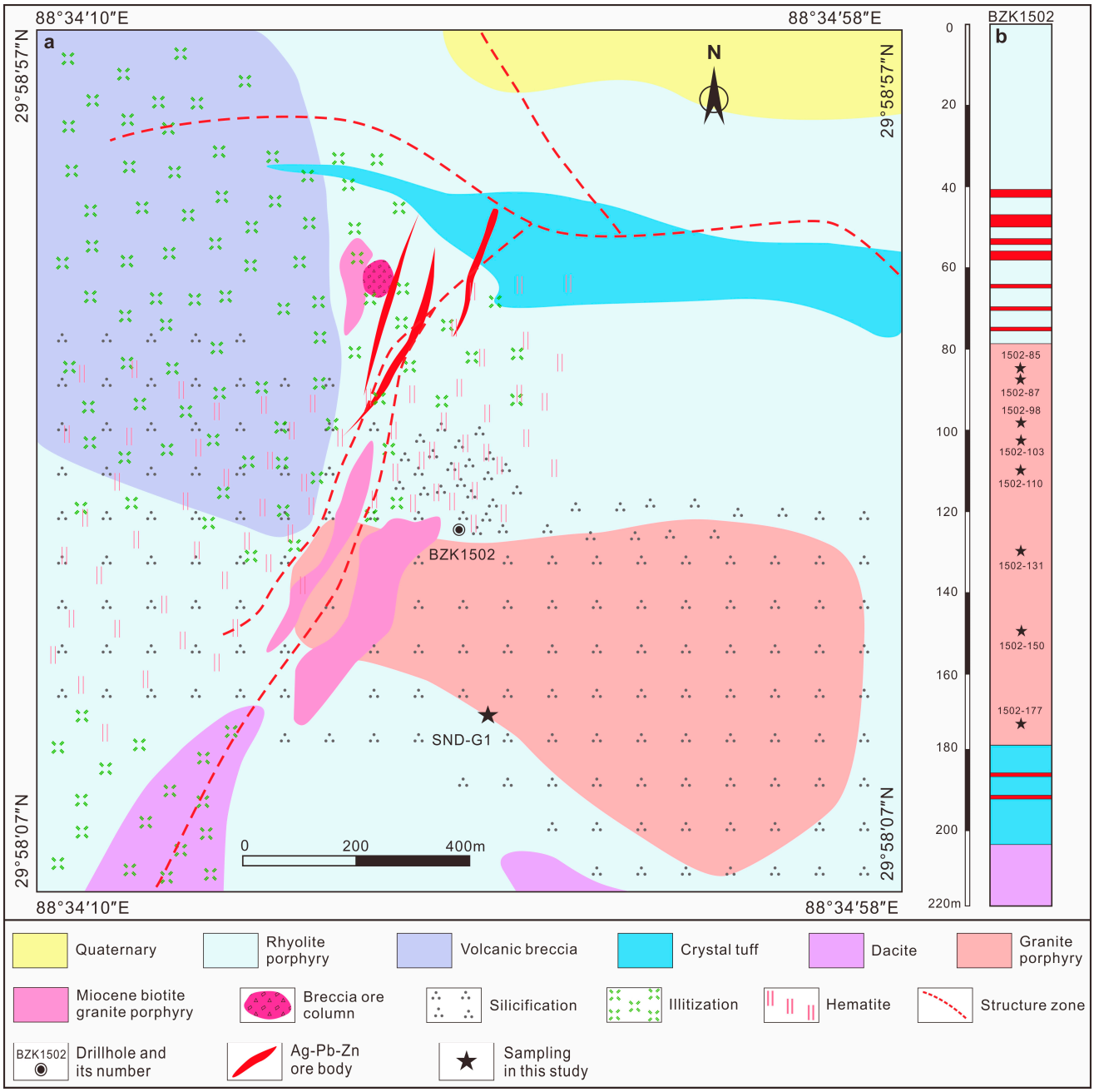


Figure 2. The simplified geological map (**a**) and lithostratigraphy of borehole BZK1502 (**b**) of the Sinongduo deposit (modified after [20]).

Mineralization is characterized by hypogene Ag-Pb-Zn sulfides, with sphalerite, galena, pyrite, and minor chalcopyrite being the main sulfide minerals present along with pearceite, argentite, pyrargyrite, acanthite, and traces of native silver (Figure 3c–i) [20]. Three mineralization stages have been identified based on the different minerals and their textural relationships, including the pre-ore stage, main-ore stage, and post-ore stage. The main-ore stage can be subdivided into three substages: galena ore substage, sphalerite ore substage, and silver minerals ore substage [21]. Alterations in the area are dominated by silicification, illitization, chalcedonization, sericitization, and carbonation [17], leading to the formation of alteration minerals such as illite, sericite, chalcedony, jasper, quartz, calcite, and minor kaolinite, adularia, and montmorillonite.

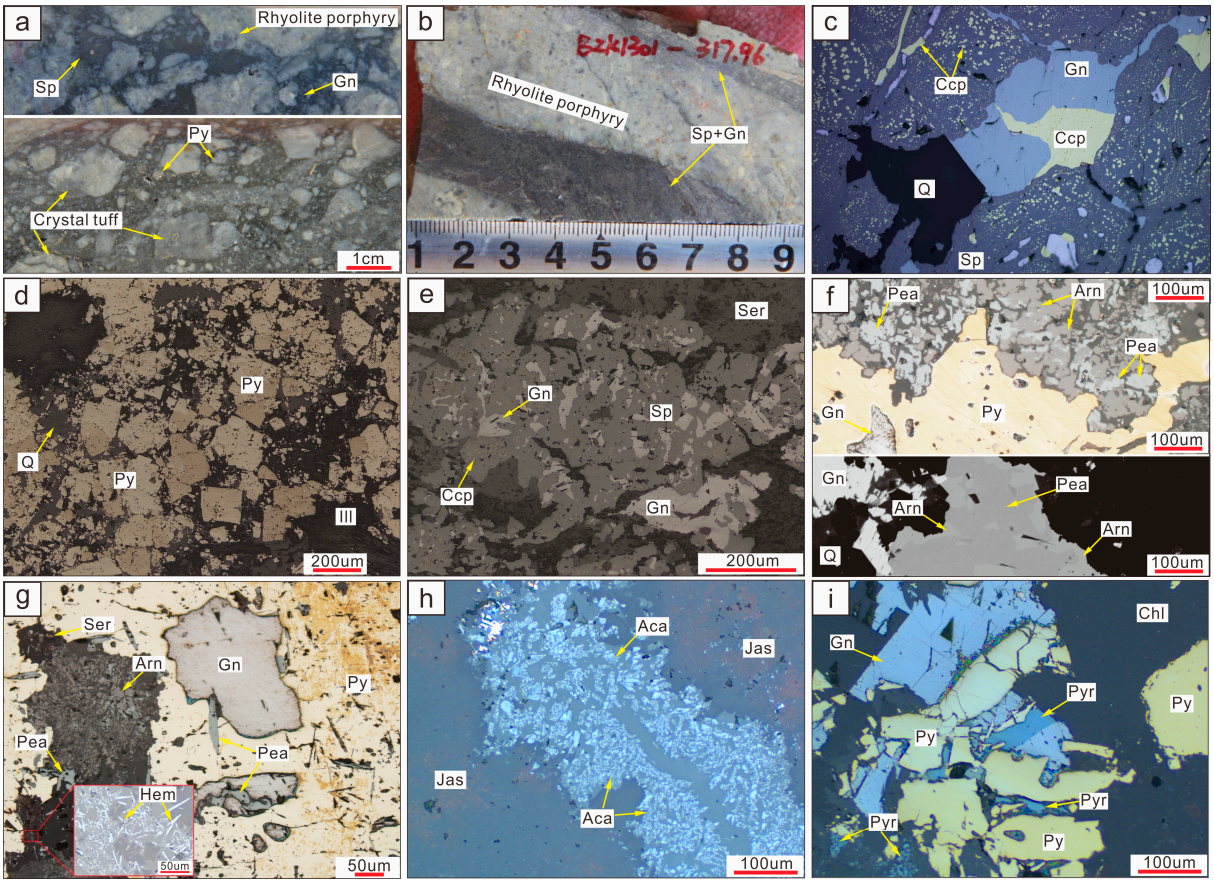


Figure 3. The hand specimen photographs and photomicrographs showing the main ore structure and textures in the mineral assemblages from the Sinongduo deposit. (**a**) The rhyolite porphyry and crystal tuff with sphalerite, galena, and pyrite sulfide minerals; (**b**) the rhyolite porphyry cut by the sphalerite–galena vein; (**c**) the chalcopyrite in the sphalerite; (**d**) the euhedral pyrite in the quartz; (**e**) the galena and sphalerite; (**f**) the pearceite and argentite; (**g**) the hematite and pearceite developed in the pyrite; (**h**) the acanthite in the jasper; (**i**) the pyrargyrite developed in pyrite fractures. Abbreviations: Sp, sphalerite; Gn, galena; Py, pyrite; Ccp, chalcopyrite; Arn, argentite; Pea, pearceite; Hem, hematite; Aca, acanthite; Pyr, pyrargyrite; Ill, illite; Jas, jasper; Ser, sericite; Chl, chlorite; Q, quartz.

4. Samples and Methods

4.1. Sample Descriptions

In this study, the borehole sample is named according to the borehole number and depth of sampling collection. Eight granite porphyry samples (SND-G1 to SND-G8) for the geochemical analysis were collected from the surface outcrop (88°34′35″ E~88°34′36″ E, 29°58′18″ N~29°58′20″ N) (Figure 2a). Eight samples (1502-85, 1502-87, 1502-98, 1502-103, 1502-110, 1502-131, 1502-150, 1502-177) were collected at different depths from the borehole BZK1502 (Figure 2b). All the granite porphyry samples studied here were gathered for further examination, with most exhibiting weak sericitization and silicification. These granite porphyries range in color from gray to white, displaying a porphyritic texture and a solid structure (Figure 4a,b). The dominant phenocryst minerals consist of potassium feldspar (15%–20%) and quartz (20%–25%), along with trace amounts of biotite (<2%). The diameter of potassium feldspar is about 0.3–1.0 mm, accompanied by weak sericitization (Figure 4c,d). The anhedral quartz grains are 0.2–0.5 mm in diameter, while biotite forms dark elongated crystals measuring 0.2–0.3 mm in length (Figure 4e). Phenocrysts are typically dispersed within a matrix of felsic minerals, primarily comprising quartz (20%–25%)

and potassium feldspar (10%), alongside a minor percentage of biotite (3%). The accessory minerals mainly include apatite, magnetite, zircon, and titanite.

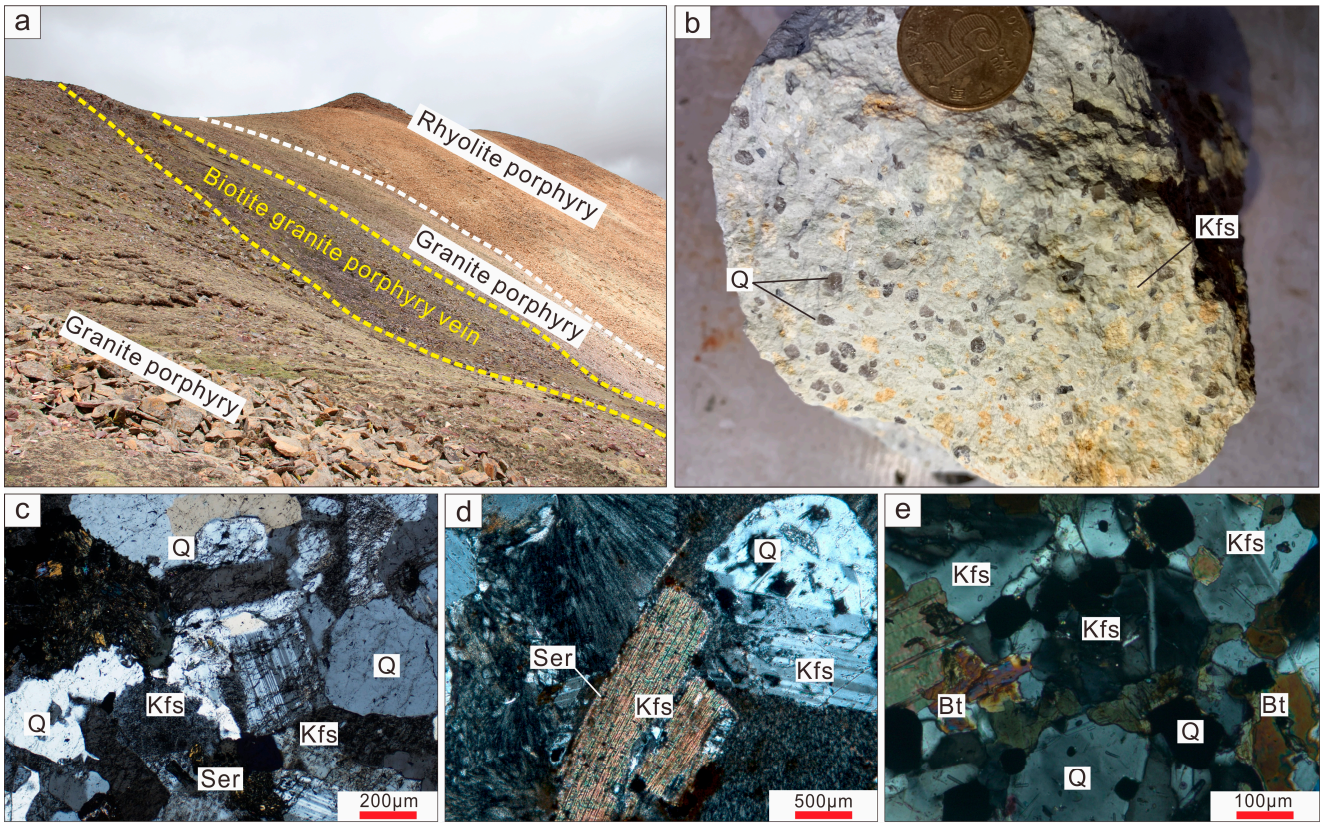


Figure 4. (**a**) The field relationship of rocks, (**b**) hand specimen photograph, and (**c**–**e**) cross-polarized photomicrographs of the granite porphyry in the Sinongduo deposit. Abbreviations: Kfs—potassium feldspar; Q—quartz; Ser—sericite; Bt—biotite.

4.2. Analytical Methods

Following petrographic analysis, two examples of granite porphyry (1502-98 and SND-G1) were chosen for zircon U-Pb dating utilizing laser ablation inductively coupled plasma mass spectrometry (LA-ICP-MS). Zircons were selected, employing standard procedures to crush the rocks and concentrate zircons via heavy liquid and magnetic techniques. Subsequently, pure zircons were handpicked under a binocular microscope at the Laboratory of the Geological Team of Hebei Province, Langfang, China. Cathodoluminescence (CL) images were captured at the Electron Microprobe Laboratory, Chinese Academy of Geological Sciences (CAGS), Beijing, using an operating voltage of 15 kV and a current of 4 nA. Zircon U-Pb isotope analyses were performed using LA-ICP-MS at the State Key Laboratory of Geological Processes and Mineral Resources, China University of Geosciences, Beijing, China. The calibration of the zircon U-Pb isotope ratio was carried out with the Zircon 91500 external standard, with NIST 610 glass serving as the reference standard and ^{29}Si used as an internal standard for U, Th, and Pb calibration. The analytical procedures closely followed those outlined in previous studies [62,63].

Sixteen samples were chosen for analysis in this study, with major and trace elements examined using whole-rock analysis methods. The samples were processed at the Analytical Laboratory of the Beijing Research Institute of Uranium Geology in China. To prepare the samples, they were pulverized down to a size of less than 200 mesh using an agate ring mill for consistency and accuracy. The major element concentrations were analyzed from fused glass disks of powdered samples using an AB104L and Axios-mAX sequential X-ray Fluorescence Spectrom. The accuracy of major elements was better than ±1%. Trace ele-

ments were analyzed using an ELEMENT 2-XR ICPMS system on solutions FeO by titrating with potassium dichromate solution. See [64] for the detailed analytical procedures.

The isotopic compositions of the whole-rock samples were determined using an ISOPROBE-T system. The separation of Sr was achieved using the DCTA complex, while Nd was separated from the REE fractions using cation-exchange resin and α-HIBA as the eluent. Mass fractionation corrections were made for the $^{87}Sr/^{86}Sr$ and $^{143}Nd/^{144}Nd$ ratios using known reference values. During the analyses, the mean $^{87}Sr/^{86}Sr$ ratio of the NBS987 standard sample was 0.710250 ± 7, and the mean $^{143}Nd/^{144}Nd$ ratio of the JMC standard sample was 0.512109 ± 3 [65]. The analytical procedures for Sr-Nd isotopic analysis used in this study were similar to those described by [66].

5. Results

5.1. Zircon U-Pb Ages

Zircons extracted from two granite porphyry samples (SND-G1 and 1502-98) were studied in order to determine their geological ages. The analysis, which included cathodoluminescence (CL) imaging, revealed that most zircon grains exhibited variable narrow oscillatory zones (Figure 5a,b), while a few grains had a homogeneous internal structure. The zircon LA-ICP-MS U-Pb analytical data can be found in Table S1, with corresponding concordia and weighted mean diagrams shown in Figure 6. Additionally, the zircon crystals exhibited Th concentrations ranging from 286 to 5963 ppm and U concentrations ranging from 208 to 2792 ppm, resulting in Th/U ratios of 0.6 to 6.4 (average value of 1.7), indicating a magmatic origin [67,68]. Consequently, the ages of the zircons are likely indicative of the crystallization ages of the granite porphyry.

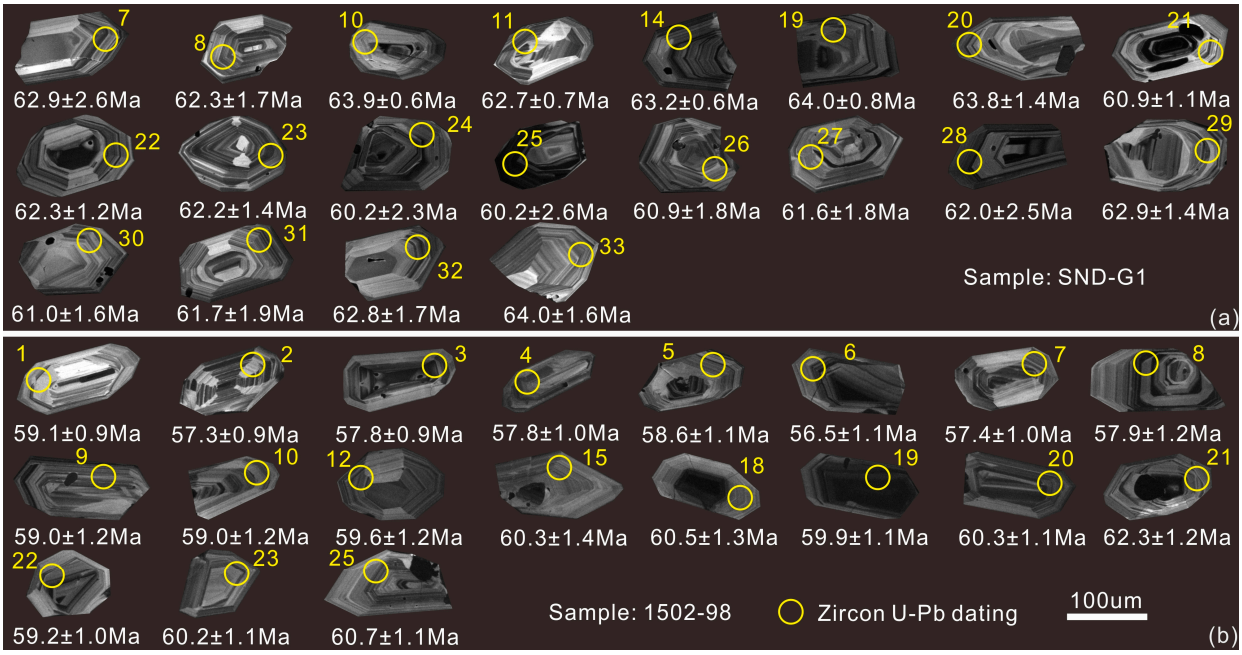


Figure 5. Representative cathodoluminescence images of zircon grains for the (**a**) SND-G1 and (**b**) 1502-98 granite porphyry samples from the Sinongduo deposit. The yellow circles are 32 μm in diameter and show the location of the U-Pb analytical sites.

A total of 20 zircon spots from sample SND-G1 showed ^{207}Pb corrected $^{206}Pb/^{238}U$ ages ranging from 60.2 ± 2.3 to 64.0 ± 1.6 Ma, with a weighted mean age of 62.9 ± 0.5 Ma (MSWD = 0.8) (Supplementary Table S1; Figure 6a,b). The analyses were mostly concordant, indicating relatively accurate results for the sample. Similarly, sample 1502-98 yielded 19 concordant analyses with ^{207}Pb-corrected $^{206}Pb/^{238}U$ ages varying from 56.5 ± 1.1 to 62.3 ± 1.2 Ma and a weighted mean age of 59.0 ± 0.7 Ma (MSWD = 1.8) (Table S1; Figure 6c,d).

Both samples have similar age ranges and dating accuracies, despite a slightly higher MSWD value for sample 1502-98 compared to SND-G1.

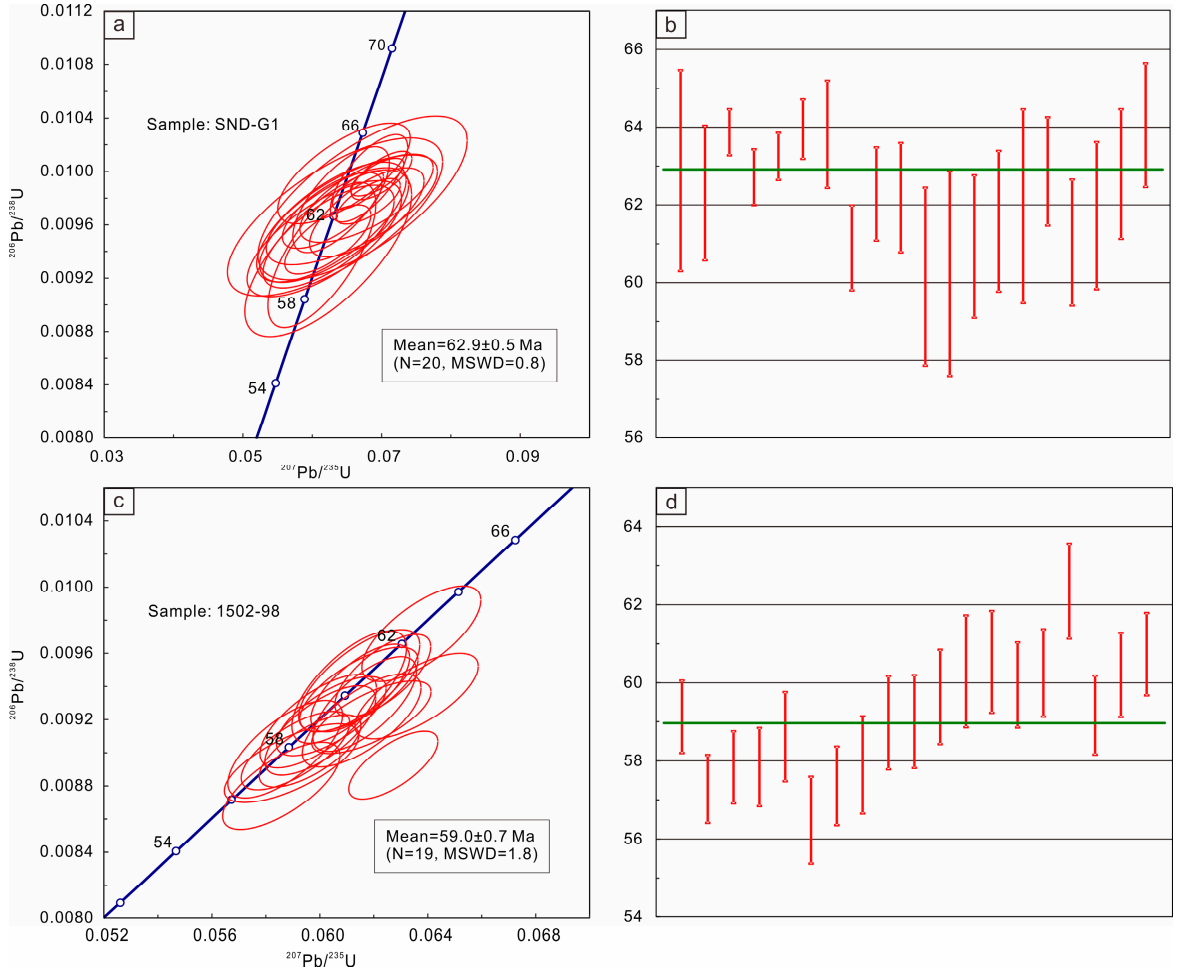


Figure 6. LA-ICP-MS zircon U-Pb concordia and weighted mean age diagrams of samples (**a**,**b**) SND-G1 and (**c**,**d**) 1502-98 for the Sinongduo granite porphyry.

5.2. Whole-Rock Geochemistry

Bulk-rock chemical compositions of the analyzed granite porphyry samples are listed in Supplementary Table S2. The granite porphyry samples analyzed in this study exhibit varying degrees of alteration as indicated by field and petrographical observations (Figure 4), along with varying loss on ignition (LOI) values ranging from 1.31 to 2.97 wt.% (Table S2). These granite porphyry samples displayed high SiO_2 (74.47–79.06 wt.%) and K_2O (4.32–4.97 wt.%), moderate Al_2O_3 (9.08–14.15 wt.%), and uniformly low Na_2O (0.65–1.88 wt.%), CaO (0.02–0.98 wt.%), and FeO^T (1.33–1.76 wt.%), contributing to total alkalis ($Na_2O + K_2O$) values between 5.32 and 6.74 wt.%. Additionally, the samples contained low levels of Fe_2O_3 (0.11–0.38 wt.%) and MgO (0.15–0.32 wt.%), with low contents of Cr (5.16–7.82 ppm) and Ni (1.95–3.32 ppm). The granite porphyries plot within the granite fields on the total alkalis versus silica (TAS) diagram (Figure 7a). The alumina saturation index (ASI = mol. $Al_2O_3/(CaO + Na_2O + K_2O)$ values of these rocks are in the range of 1.08–2.00, suggesting that they are strongly peraluminous series (Figure 7b).

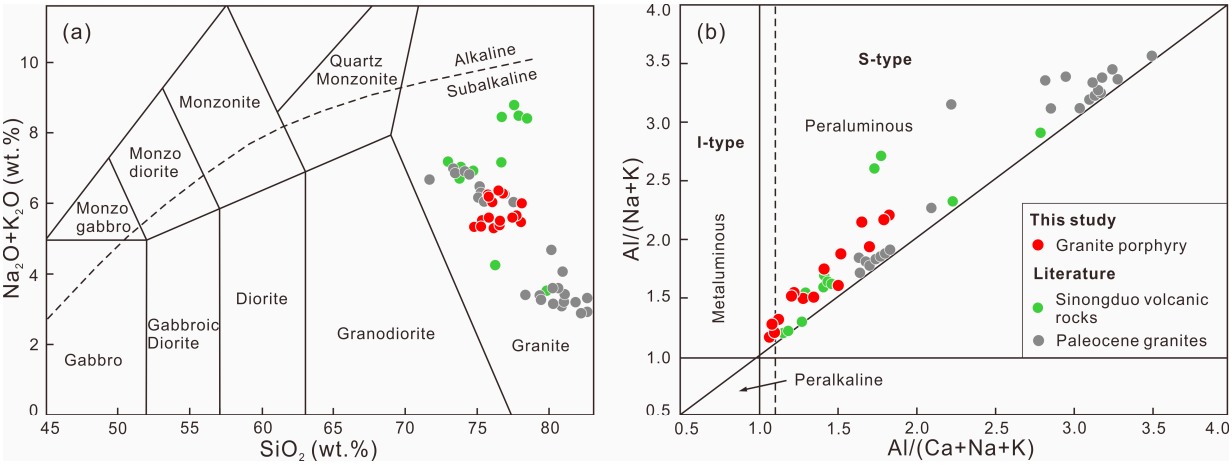


Figure 7. Geochemical diagrams for the granite porphyry from the Sinongduo deposit. (**a**) SiO_2 versus $Na_2O + K_2O$ diagram after [69]; (**b**) A/NK versus A/CNK diagram after [70]. Data for the Sinongduo volcanic rocks are from [71]; data for the Paleocene granites are from [72].

The total REE concentrations of the samples analyzed in this study range from 114 to 217 ppm, with an average value of 158 ppm. These granite porphyries exhibit a significant enrichment in light rare earth elements (LREEs) over heavy rare earth elements (HREEs), as shown in the chondrite-normalized REE patterns (Figure 8a). Interestingly, there are no discernible Ce anomalies with Ce/Ce* ratios ranging from 0.83 to 1.12 and negative Eu anomalies with Eu/Eu* ratios from 0.23 to 0.59 (Figure 8a; Table S2). On the primitive mantle-normalized incompatible trace element patterns (Figure 8b), these samples are enriched in the large-ion lithophile elements (LILEs, e.g., Rb, Ba) and LREEs and are depleted in the high-field-strength elements (HFSEs, e.g., Nb, Ta, and Ti). The normalized REE and incompatible element abundance curves of the studied granite porphyries are similar to those of the Sinongduo volcanic rocks and Paleocene granites, indicating that they originated from similar primary magma [72].

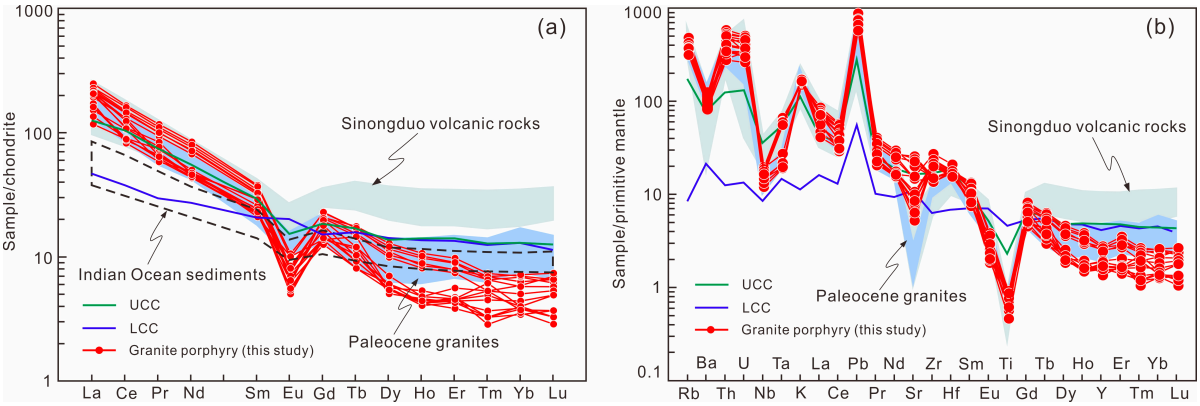


Figure 8. (**a**) The chondrite-normalized REE patterns and (**b**) primitive mantle normalized trace element patterns for the Sinongduo granite porphyry. Data for the chondrite and primitive mantle normalization are from [73], data for the Indian Ocean sediments, UCC, and LCC are from [74], Sinongduo volcanic rock data are from [71], and Paleocene granite data are from [72]. Abbreviations: UCC, upper continental crust; LCC, lower continental crust.

5.3. Sr-Nd Isotopic Compositions

The whole-rock Sr-Nd isotopic compositions of the representative samples can be found in Supplementary Table S3 and are illustrated in Figure 9. The initial Sr and Nd isotopic ratios of all the samples were determined to be 62.9 Ma and 59.0 Ma, respectively.

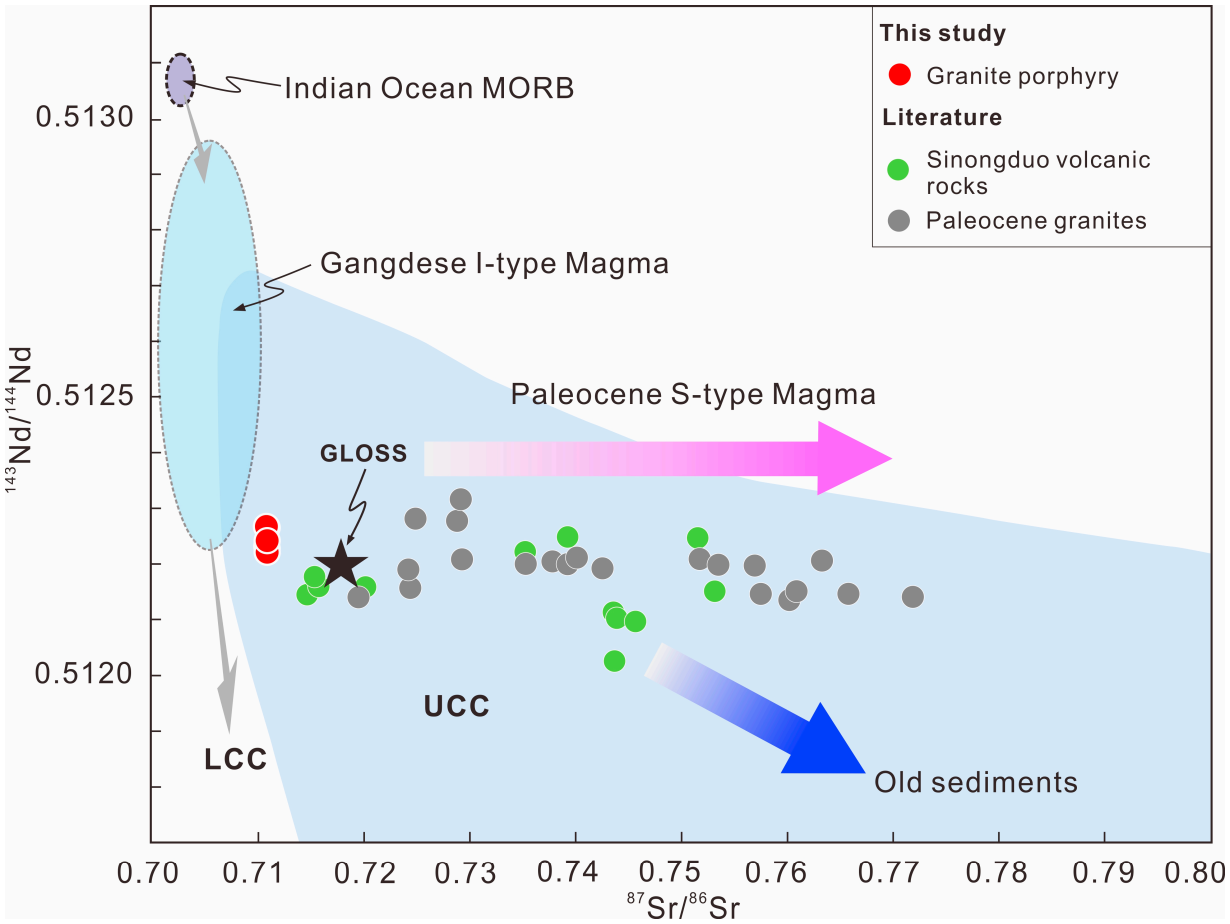


Figure 9. The Sr-Nd isotopic compositions for the granite porphyry from the Sinongduo deposit. Data for the Indian Ocean MORB, UCC, and LCC are from [75–77]. Data for global subducting sediment (GLOSS) are from [78]. Data for the Sinongduo volcanic rocks are from [71]; data for the Paleocene granites are from [72].

The six granite porphyry samples examined in this study displayed consistent whole-rock initial ratios for both ($^{87}Sr/^{86}Sr$) and ($^{143}Nd/^{144}Nd)_i$. The average ($^{87}Sr/^{86}Sr$) ratio was calculated to be 0.70841, ranging from 0.70764 to 0.70893, while the average ($^{143}Nd/^{144}Nd)_i$ ratio was 0.51219, varying between 0.51217 and 0.51222. Furthermore, all samples exhibited negative $\varepsilon_{Nd}(t)$ values that fell within a narrow range between −6.7 and −7.6, with an average value of −7.2. The calculated single-stage Nd model ages (TDM) ranged from 1106 to 1188 Ma, whereas the two-stage Nd model ages (T_{2DM}) spanned from 1413 to 1488 Ma.

6. Discussion

6.1. Timing of Magmatism and Its Link with the Ag-Pb-Zn Mineralization

The ages of the two granite porphyry samples analyzed using LA-ICP-MS zircon U-Pb dating are 62.9 ± 0.5 Ma and 59.0 ± 0.7 Ma, respectively (Figure 6a–d). This is distinct from the zircon U-Pb age of the biotite granite porphyry dated by Shi et al. (2017) (12 Ma; [79]). The Miocene biotite granite porphyry belongs to the post mineralization magmatic intrusion that plays a destructive role in the Ag-Pb-Zn ore body. The newly obtained isotopic ages in this study suggest that the granite porphyry in the Sinongduo deposit was emplaced between 59.0 and 62.9 Ma, corresponding to the Paleocene epoch. This timing coincides with the formation of ore-bearing volcanic rocks in the same deposit, such as the rhyolite porphyry (64.2–65.0 Ma), crystal tuff (62.1–65.2 Ma), volcanic breccia (63.1–64.8 Ma), and dacite (61.9–62.4 Ma) (reference [71]). Moreover, Li et al. [21] reported Ar-Ar isochron ages of 60.9 ± 0.7 Ma to 63.1 ± 0.7 Ma for the quartz-sericite-illite-sulfide veins related to

the main mineralization event. These findings indicate that the Ag-Pb-Zn mineralization in the Sinongduo deposit coincided with the emplacement of the granite porphyry and volcanics, suggesting a Paleocene age for the volcanism-magmatism and mineralization in the Sinongduo deposit. Therefore, the granite porphyry magmatic intrusion may have a genetic link between the Ag-Pb-Zn mineralizations, which likely provides the ore-forming magma for the Sinongduo deposit.

6.2. Classification of the Granite Porphyry

The granite porphyry from the Sinongduo deposit is characterized by its strong peraluminous composition and its classification within the S-type magma field (Figures 7b and 10). This sets it apart from the I-type Gangdese batholith (58–66 Ma) and coeval volcanic rocks (59–65 Ma) found in the central Lhasa terrane [72]. Moreover, the features of low 10,000*Ga/Al ratios (2.9–4.4) and Zr + Nb + Ce + Y values (237–367 ppm) indicate that the Sinongduo granite porphyries also exhibit distinctions from the A-type granites [80].

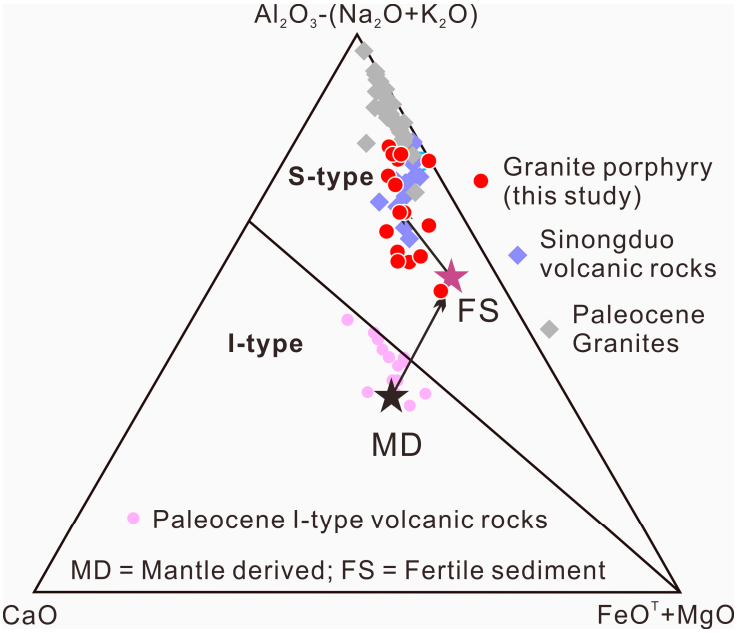


Figure 10. Al_2O_3-(Na_2O + K_2O) versus CaO versus FeO^T + MgO diagram (after [81]). Data for the Paleocene I-type volcanic rocks are from [32,33]; other data from the literature are from [10,71,72].

According to Chappell and White [81,82], S-type granites are characterized by the following: (1) high peraluminous nature with ASI > 1.1, (2) presence of more than 1% CIPW normative corundum, and (3) limited to elevated SiO_2 levels with relatively decreased Na_2O (usually less than 3.2%) but increased K_2O (around 5%) content. The composition of the Sinongduo granite porphyry indicates a composition typical of S-type granite affinity, with high SiO_2 and K_2O contents and low Na_2O content. The ASI value falling between 1.08 and 2.00 further supports this classification. The Sinongduo granite porphyries exhibit higher corundum contents, ranging from 1.07 to 7.32%, as calculated by CIPW analysis, compared to the depleted I-type series [83].

The categorization of the Sinongduo granite porphyries as S-type is further corroborated by their whole-rock initial $^{87}Sr/^{86}Sr$ isotopic ratios (ranging from 0.708 to 0.709). This is because Sr isotopes are more radiogenic in S-type granites, which typically display initial $^{87}Sr/^{86}Sr$ values greater than 0.708 [83]. In addition, as shown in the Al_2O_3-(Na_2O + K_2O) versus CaO versus FeO^T + MgO diagram (Figure 10), all the Sinongduo granite porphyries are plotted into the S-type field, similar to the Paleocene granites and Sinongduo coeval volcanic rocks (61.9–65.2 Ma).

6.3. Magma Source and Petrogenesis

Our examination of the granite porphyry samples reveals that they underwent a minor sericite alteration (Figure 4c,d). The loss-on-ignition (LOI) results indicate that the granite porphyry has a minor level of alteration, with values ranging from 1.31 to 2.97 wt.% and an average of 2.37 wt.%. The geochemical composition can be effectively used as an indicator for tracing back to the magma source because of its consistent oxide content. Furthermore, the samples display consistent trends in their rare earth element (REE) and trace element patterns (Figure 8a,b), demonstrating the maintained intrinsic geochemical properties [84].

The high SiO_2 contents observed in the Sinongduo granite porphyry samples are consistent with the chemical characteristics of high silica granites (HSGs), a classification typically reserved for granitic rocks exhibiting SiO_2 concentrations greater than 70% [83]. The HSFs are believed to originate through a direct process involving extensive fractional crystallization of their primitive mafic parent magmas [85]. The origin of peraluminous geochemistry in granite porphyry is an important question that needs consideration. It is crucial to determine whether this geochemistry originated directly from the source region or if it developed through processes such as assimilation and fractional crystallization (AFC) from a more mafic parent rock [86]. Previous studies have shown that the Dianzhong volcanic rocks belong to the I-type rocks that are formed from a combination of mantle wedge materials and a crustal component via the AFC processes [8,10,35]. However, the Sinongduo granite porphyry display notably low concentrations of CaO (0.02–0.98 wt.%), MgO (0.15–0.32 wt.%), Na_2O (0.65–1.88 wt.%), FeO^T (1.33–1.76 wt.%), Ni (1.95–3.32 ppm), Cr (5.16–7.82 ppm), and Co (2.65–4.01 ppm), along with a radiogenic Sr isotope composition, in contrast to the Dianzhong I-type series [35,87]. Therefore, it is suggested that the magma source of these granite porphyries is unlikely to be linked to partial melting processes of either the mantle wedge or the mafic lower continental crust (LCC).

Moreover, the initial ratios of $^{87}Sr/^{86}Sr$ ratios and $\varepsilon_{Nd}(t)$ in the granite porphyries do not exhibit a reliable correlation with SiO_2 concentrations (Figure 11a,b), thus hindering substantial crustal assimilation. In terms of fractional crystallization, high-field-strength elements like Zr, Ta, and Nb are employed to determine the extent of fractional crystallization [88]. The concentrations of Nb and Ta are positively correlated with the extent of fractional crystallization, suggesting that as more fractional crystallization occurs, the concentrations of these elements increase. Conversely, the ratios of Nb/Ta and Zr concentration decrease as the process of fractional crystallization progresses [88]. The Nb/Ta ratios observed in the Sinongduo granite porphyry resemble those found in the upper continental crust (UCC) but differ from the lower continental crust (LCC) or basin continental crust (UCC) (Figure 11c,d), indicating that these granite porphyries did not undergo strongly fractional crystallization and the geochemistry of these magmatic rocks mirrors the composition of their source region.

All the studied granite porphyries exhibit nearly overlapping patterns with that of the UCC (Figure 8a,b), suggesting higher levels of LREE compared to the LCC and Indian Ocean sediments. It is observed that the granite porphyries exhibit notable negative Eu anomalies (Eu/Eu* = 0.23 to 0.59, Figure 8a). This trend is consistent with the Eu anomalies of the UCC (average Eu/Eu* = 0.65) [89] but contrasts with the positive Eu anomalies of the LCC (average Eu/Eu* = 1.14) [88], which suggests a distinct geochemical signature that aligns more closely with the UCC than the LCC. Additionally, the Sr-Nd isotope compositions of the granite porphyry rocks, including the Sinongduo volcanic rocks and Paleocene granitoids, are within the field of the UCC, suggesting UCC affinity (Figure 9).

In conclusion, it is proposed that the Sinongduo granite porphyry originated from a sedimentary upper continental crust source due to its geochemical similarities with the upper continental crust. This suggests that these rocks were formed through melting processes associated with the UCC rather than from the more mafic lower continental crust or oceanic crust.

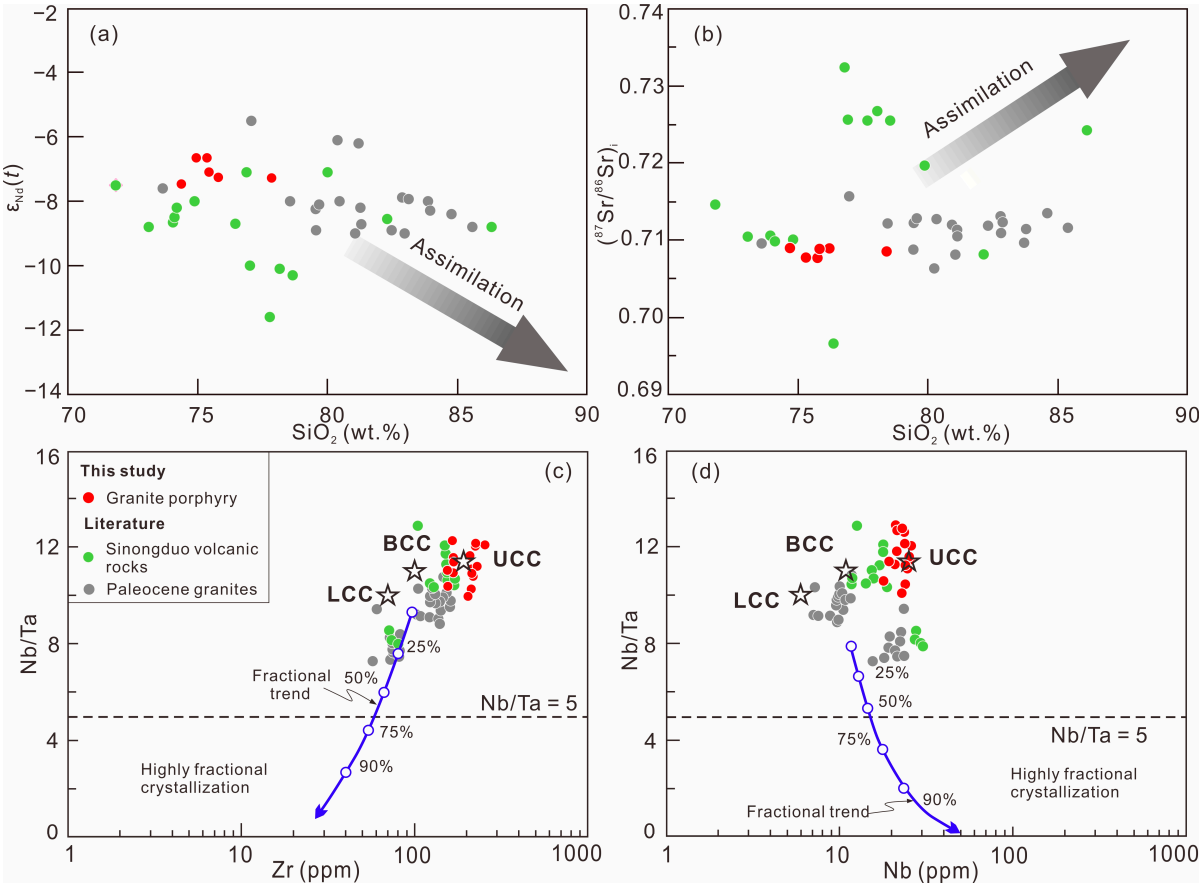


Figure 11. (**a**) SiO_2 versus $\varepsilon_{Nd}(t)$, (**b**) SiO_2 versus $(^{87}Sr/^{86}Sr)_i$, (**c**) Nb/Ta versus Zr, and (**d**) Nb/Ta versus Nb diagrams (after [88]. Data for the BCC are from [74]; other data sources are the same as that in the Figure 9. Abbreviations: UCC, upper continental crust; LCC, lower continental crust; BCC, basin continental crust.

6.4. Tectonic Implications

Previous studies have mainly proposed three potential scenarios for the S-type granitic rocks: (1) crustal anatexis [90], (2) crustal extension [91], and (3) extraction from the shallow andesitic magma via fractional crystallization process [92]. Barbarin (1999) suggested the necessity of a deeply buried metasedimentary source for the formation of S-type magma through crustal anatexis [93]. Moreover, the thickened crust mechanism could be accountable for the development of highly peraluminous S-type granites in the post-collisional tectonic environment [93,94].

Most published studies have supported that the collision ages of India–Asia range from Late Cretaceous to Oligocene and that the onset collision age is 55 ± 5 Ma [95,96], showing a collisional tectonic setting [36]. In the Paleocene, the Lhasa terrane was situated in a collisional rather than post-collisional tectonic setting [93], making it inappropriate to link the rocks with post-collisional highly peraluminous S-type granites. In addition, a two-stage rollback of the subducted oceanic crust was proposed by Collins and Richards [91] to induce a crustal extension mechanism for the formation of S-type granite, which is linked to high temperature and low-pressure metamorphic complexes, as well as a considerable transient heat influx to the crust. However, the Sinongduo magmatic and volcanic rocks lack such metamorphic complexes. Therefore, the crustal extension mechanism cannot be attributed to the Sinongduo granite porphyry. Additionally, the extraction mechanism from the andesitic magma through fractional crystallization process cannot be applicable due to the low degree of fractional crystallization observed in the investigated granite porphyries.

7. Conclusions

(1) LA-ICP-MS zircon U-Pb age shows that the granite porphyry was formed at 59.0–62.9 Ma, consistent with the timing of the mineralization, indicating that the granite porphyry intrusion is most likely the ore-forming magma in the Sinongduo deposit.
(2) The geochemical and isotopic data suggest that the granite porphyry was a strongly peraluminous series which belongs to S-type granite.
(3) The geochemical and isotopic characteristics of the granite porphyry are similar to those of the upper continental crust, which implies that the granite porphyry from the Sinongduo deposit likely originated from the melting of the upper continental crust in the India–Asia collisional tectonic setting.

Supplementary Materials: The following supporting information can be downloaded at https://www.mdpi.com/article/10.3390/min14070710/s1: Table S1. LA-ICP-MS zircon U-Pb isotopic analyses for the granite porphyries from the Sinongduo deposit; Table S2. Major oxides (wt.%) and trace element (ppm) compositions for the Sinongduo granite porphyries; Table S3. Whole-rock Sr-Nd isotopic compositions for the granite porphyry in Sinongduo deposit.

Author Contributions: Writing—original draft preparation, P.Z. and Z.L.; funding acquisition, Z.L. and F.Z.; investigation and methodology, Z.L.; supervision, F.Z. and X.L. All authors have read and agreed to the published version of the manuscript.

Funding: This research was financially supported by the Natural Science Foundation of Sichuan Province (2023NSFSC0783), the Opening Foundation of State Key Laboratory of Continental Dynamics, Northwest University (23LCD01), and the National College Student Innovation and Entrepreneurship Training Project (X2023006).

Data Availability Statement: Our research data can be found in Supplementary Materials.

Acknowledgments: We thank the three anonymous reviewers for their constructive comments and suggestions to further improve this manuscript.

Conflicts of Interest: The authors declare no conflicts of interest.

References

1. Hou, Z.Q.; Wang, R.; Zhang, H.J.; Zheng, Y.C.; Jin, S.; Thybo, H.; Weinberg, R.F.; Yang, Z.M.; Hao, A.W.; Gao, L.; et al. Formation of giant copper deposits in Tibet driven by treating of the subducted Indian plate. *Earth Sci. Rev.* **2023**, *243*, 104482. [CrossRef]
2. Jadoon, U.F.; Zhao, Q.; Huang, B.C.; Yi, Z.Y.; Azeem, M.W.; Lu, H.L.; Shah, S.A. A review of paleomagnetic constraints on the India-Asia collision: Paradoxes and perspectives. *Earth Sci. Rev.* **2024**, *248*, 104628. [CrossRef]
3. Wang, R.; Weinberg, R.F.; Collins, W.J.; Richards, J.P.; Zhu, D.C. Origin of postcollisional magmas and formation of porphyry Cu deposits in southern Tibet. *Earth Sci. Rev.* **2018**, *181*, 122–143. [CrossRef]
4. Yin, A.; Harrison, T.M. Geologic evolution of the Himalayan–Tibetan orogen. *Annu. Rev. Earth Planet. Sci.* **2000**, *28*, 211–280. [CrossRef]
5. Lang, X.H.; Deng, Y.L.; Wang, X.H.; Tang, J.X.; Yin, Q.; Xie, F.W.; Jiang, K. Geochronology and geochemistry of volcanic rocks of the Bima Formation, southern Lhasa subterrane, Tibet: Implications for early Neo-Tethyan subduction. *Gondwana Res.* **2020**, *80*, 335–349. [CrossRef]
6. Pan, G.T.; Mo, X.X.; Zhu, D.C.; Wang, L.Q.; Li, G.M.; Zhao, Z.D.; Zhang, L. Spatial-temproral framework of the orogenic belt and its evolution. *Acta Petrol. Sin.* **2006**, *22*, 521–533, (In Chinese with English Abstract).
7. Zhu, D.C.; Zhao, Z.D.; Niu, Y.; Mo, X.X.; Chung, S.L.; Hou, Z.Q.; Wu, F.Y. The Lhasa Terrane: Record of a microcontinent and its histories of drift and growth. *Earth Planet. Sci. Lett.* **2011**, *301*, 241–255. [CrossRef]
8. Lee, H.Y.; Chung, S.L.; Lo, C.H.; Ji, J.Q.; Lee, T.Y.; Qian, Q.; Zhang, Q. Eocene Neotethyan slab breakoff in southern Tibet inferred from the Linzizong volcanic record. *Tectonophysics* **2009**, *477*, 20–35. [CrossRef]
9. Zhang, S.H.; Ji, W.Q.; Chen, H.B.; Kirstein, L.A.; Wu, F.Y. Linking rapid eruption of the Linzizong volcanic rocks and early Eocene climatic optimum (EECO): Constraints from the Pana formation in the Linzhou and Pangduo basins, southern Tibet. *Lithos* **2023**, *446–447*, 107159. [CrossRef]
10. Mo, X.X.; Hou, Z.Q.; Niu, Y.L.; Dong, G.C.; Qu, X.M.; Zhao, Z.D.; Ke, S. Contribution of syncollisional felsic magmatism to continental crust growth: A case study of the Paleogene Linzizong volcanic succession in southern Tibet. *Chem. Geol.* **2008**, *250*, 49–67. [CrossRef]
11. Jiang, X.J.; Ma, Y.; Kang, Y.M.; Yi, J.Z.; Yan, J.; Gao, S.B.; Chen, L.; Zheng, Y.Y. Determining multiple fluid pulse and evolution using zoned garnet in Mengya'a skarn Pb-Zn-polymetallic deposit, Tibet. *Ore Geol. Rev.* **2023**, *163*, 105795. [CrossRef]

12. Xu, J.; Zheng, Y.Y.; Sun, X.; Li, X.F.; Mao, G.Z. Genesis of the Yaguila Pb-Zn-Ag-Mo skarn deposit in Tibet: Insights from geochronology, geochemistry, and fluid inclusions. *J. Asian Earth Sci.* **2019**, *172*, 83–100. [CrossRef]
13. Hou, Z.Q.; Duan, L.F.; Lu, Y.J.; Zheng, Y.C.; Zhu, D.C.; Yang, Z.M.; Yang, Z.S.; Wang, B.D.; Pei, Y.R.; Zhao, Z.D.; et al. Lithospheric architecture of the Lhasa Terrane and its control on ore deposits in the Himalayan-Tibetan Orogen. *Econ. Geol.* **2015**, *110*, 1541–1575. [CrossRef]
14. Qin, Q.; Zhong, L.L.; Zhong, K.H.; He, Z.Y.; Yan, Z.; Dewaele, S.; Peng, J.; Zhang, H.J.; Grave, J.D.; Su, W.B.; et al. Structural setting of the Narusongduo Pb-Zn ore deposit in the Gangdese belt, central Tibet. *Ore Geol. Rev.* **2022**, *143*, 104748. [CrossRef]
15. Tang, J.X.; Wang, Q.; Yang, C.; Lang, X.H.; Li, H.F.; Huang, Y.R.; Yang, H.H. Two porphyry-epithermal deposit metallogenic subseries in Tibetan Plateau: Practice of "absence prospecting" deposit metallogenic series. *Miner. Depos.* **2014**, *6*, 1151–1170. (In Chinese with English Abstract)
16. Guo, N.; Liu, D.; Tang, J.X.; Zheng, L.; Huang, Y.R.; Shi, W.X.; Fu, Y.; Tang, N.; Wang, C. Characteristics of alteration minerals and prospecting model revealed by shortwave infrared technique: Take Sinongduo Ag-Pb-Zn deposit as an example. *Miner. Depos.* **2018**, *37*, 556–570. (In Chinese with English Abstract)
17. Guo, N.; Guo, W.B.; Shi, W.X.; Huang, Y.R.; Guo, Y.N.; Lian, D.M. Characterization of illite clays associated with the Sinongduo low sulfidation epithermal deposit, Central Tibet using field SWIR spectrometry. *Ore Geol. Rev.* **2019**, *120*, 103228. [CrossRef]
18. Huang, Y.R.; Guo, N.; Zheng, L.; Yang, Z.Y.; Fu, Y. 3D geological alteration mapping based on remote sensing and shortwave infrared technology: A case study from the Sinongduo low sulfidation epithermal deposit. *Acta Geosci. Sin.* **2017**, *38*, 779–789. (In Chinese with English Abstract)
19. Lang, X.H.; Tang, J.X.; Yang, Z.Y.; Ding, S.; Hu, G.Y.; Li, Y.H.; Yan, C.M. Geophysical characteristics and prospecting direction of the Sinongduo Pb-Zn deposit in Xietongmen county, Tibet. *Geol. Explor.* **2017**, *53*, 0508–0518. (In Chinese with English Abstract)
20. Li, Z.; Lang, X.H.; Ding, S.; Li, H.F.; Yang, Z.Y.; Shi, S.; Li, Y.H. A study of the modes of occurrence of silver in the Sinongduo epithermal Ag-Pb-Zn deposit, Tibet. *Acta Geosci. Sin.* **2017**, *38*, 687–701. (In Chinese with English Abstract)
21. Li, H.F.; Tang, J.X.; Hu, G.Y.; Ding, S.; Li, Z.; Xie, F.W.; Teng, L.; Cui, S.Y. Fluid inclusions, isotopic characteristics and geochronology of the Sinongduo epithermal Ag-Pb-Zn deposit, Tibet, China. *Ore Geol. Rev.* **2019**, *107*, 692–706. [CrossRef]
22. Tang, J.X.; Ding, S.; Meng, Z.; Hu, G.Y.; Gao, Y.M.; Xie, F.W.; Fu, Y.G. The first discovery of the low sulfidation epithermal deposit in Linzizong volcanics, Tibet: A case study of the Sinongduo Ag polymetallic deposit. *Acta Geosci. Sin.* **2016**, *37*, 461–470. (In Chinese with English Abstract)
23. Wang, M.; Li, C.; Dong, Y.S.; Jiang, W.; Jie, C.M.; Wu, Y.W. Cenozoic thrusting nappe structure in the Sinongduo area, Xietongmen, Tibet, China. *Geol. Bull. China* **2010**, *29*, 1851–1856. (In Chinese with English Abstract)
24. Yang, Z.Y.; Zhang, C.H.; Zhao, X.Y.; Lang, X.H.; Xiao, H.T.; Liang, J. Characteristics of rock geochemical anomalies and prospecting potential of the Sinongduo silver polymetallic deposit, Tibet. *Geophys. Geochem. Explor.* **2019**, *43*, 702–708. (In Chinese with English Abstract)
25. Zhu, D.C.; Zhao, Z.D.; Niu, Y.L.; Dilek, Y.; Hou, Z.Q.; Mo, X.X. The origin and preCenozoic evolution of the Tibetan Plateau. *Gondwana Res.* **2013**, *23*, 1429–1454. [CrossRef]
26. Dong, X.; Zhang, Z.M.; Santosh, M.; Wang, W.; Yu, F.; Liu, F. Late Neoproterozoic thermal events in the northern Lhasa terrane, south Tibet: Zircon chronology and tectonic implications. *J. Geodyn.* **2011**, *52*, 389–405. [CrossRef]
27. Zhang, Z.M.; Zhao, G.C.; Santosh, M.; Wang, J.L.; Dong, X.; Shen, K. Late Cretaceous charnockite with adakitic affinities from the Gangdese batholith, southeastern Tibet: Evidence for Neo-Tethyan mid-ocean ridge subduction? *Gondwana Res.* **2010**, *17*, 615–631. [CrossRef]
28. Lang, X.H.; Wang, X.H.; Deng, Y.L.; Tang, J.X.; Xie, F.W.; Yang, Z.Y.; Jiang, K. Hydrothermal evolution and ore precipitation of the No. 2 porphyry Cu–Au deposit in the Xiongcun district, Tibet: Evidence from cathodoluminescence, fluid inclusions, and isotopes. *Ore Geol. Rev.* **2019**, *114*, 103141. [CrossRef]
29. Wang, R.; Richards, J.P.; Zhou, L.M.; Hou, Z.Q.; Stern, R.A.; Creaser, R.A.; Zhu, J.J. The role of Indian and Tibetan lithosphere in spatial distribution of Cenozoic magmatism and porphyry Cu-Mo deposits in the Gangdese belt, southern Tibet. *Earth Sci. Rev.* **2015**, *150*, 68–94. [CrossRef]
30. Kang, Z.Q.; Xu, J.F.; Wilde, S.A.; Feng, Z.H.; Chen, J.L.; Wang, B.D.; Fu, W.C.; Pan, H.B. Geochronology and geochemistry of the Sangri Group Volcanic Rocks, Southern Lhasa Terrane: Implications for the early subduction history of the NeoTethys and Gangdese Magmatic Arc. *Lithos* **2014**, *200–201*, 157–168. [CrossRef]
31. Wei, Y.Q.; Zhao, Z.D.; Niu, Y.L.; Zhu, D.C.; Liu, D.; Wang, Q.; Wei, J.C. Geochronology and geochemistry of the Early Jurassic Yeba Formation volcanic rocks in southern Tiebet: Initiation of back-arc rifting and crustal accretion in the southern Lhasa Terrane. *Lithos* **2017**, *278–281*, 477–490. [CrossRef]
32. Mo, X.X.; Zhao, Z.D.; Deng, J.F.; Dong, G.C.; Zhou, S.; Guo, T.Y.; Zhang, S.Q.; Wang, L.L. Response of volcanism to the India–Asia collision. *Earth Sci. Front. China Univ. Geosci. Beijing* **2003**, *10*, 135–147, (In Chinese with English Abstract).
33. Lee, H.Y.; Chung, S.L.; Ji, J.Q.; Qian, Q.; Gallet, S.; Lo, C.H.; Zhang, Q. Geochemical and Sr–Nd isotopic constraints on the genesis of the Cenozoic Linzizong volcanic successions, southern Tibet. *J. Asian Earth Sci.* **2012**, *53*, 96–114. [CrossRef]
34. Dong, G.C.; Mo, X.X.; Zhao, Z.D.; Wang, L.L.; Zhou, S. A new understanding of the stratigraphic successions of the Linzizong volcanic rocks in the Linzhou basin, Tibet. *Geol. Bull. China* **2005**, *24*, 549–557, (In Chinese with English Abstract).
35. Mo, X.X.; Hou, Z.Q.; Niu, Y.L.; Dong, G.C.; Qu, X.M.; Zhao, Z.D.; Yang, Z.M. Mantle contributions to crustal thickening in south Tibet in response to the India–Asia collision. *Lithos* **2007**, *96*, 225–242. [CrossRef]

36. Zhu, D.C.; Wang, Q.; Zhao, Z.D.; Chung, S.L.; Cawood, P.A.; Niu, Y.L.; Mo, X.X. Magmatic record of India-Asia collision. *Sci. Rep.* **2015**, *5*, 14289. [CrossRef]
37. Coulon, C.; Maluski, H.; Bollinger, C.; Wang, S. Mesozoic and Cenozoic volcanic rocks from central and southern Tibet: ^{39}Ar–^{40}Ar dating, petrological characteristics and geodynamical significance. *Earth Planet. Sci. Lett.* **1986**, *79*, 281–302. [CrossRef]
38. Xu, R.H.; Schärer, U.; Allègre, C.J. Magmatism and metamorphism in the Lhasa block (Tibet): A geochronological study. *J. Geol.* **1985**, *93*, 41–57. [CrossRef]
39. He, S.D.; Kapp, P.; DeCelles, P.G.; Gehrels, G.E.; Heizler, M. Cretaceous-Tertiary geology of the Gangdese Arc in the Linzhou area, southern Tibet. *Tectonophysics* **2007**, *433*, 15–37. [CrossRef]
40. Zhu, D.C.; Wang, Q.; Cawood, P.A.; Zhao, Z.D.; Mo, X.X. Raising the Gangdese Mountains in southern Tibet. *J. Geophys. Res. Solid Earth* **2017**, *122*, 214–223. [CrossRef]
41. Harris, N.B.W.; Xu, R.; Lewis, C.L.; Jin, C.W. Plutonic rocks of the 1985 Tibet Geotraverse, Lhasa to Golmud. *Philos. Trans. R. Soc. Lond.* **1988**, *A327*, 145–168.
42. Mo, X.X.; Dong, G.C.; Zhao, Z.D.; Guo, T.Y.; Wang, L.L.; Chen, T. Timing of magma mixing in Gangdise magmatic belt during the India–Asia collision: Zircon SHIRMP U–Pb dating. *Acta Geol. Sin.* **2005**, *79*, 66–76.
43. Chen, X.L.; Liang, H.Y.; Zhang, J.; Sotiriou, P.; Huang, W.T.; Ren, L.; Zhang, L.; Zou, Y.Q. Geochemical characteristics and magma fertility for the Jurassic arc rocks in the Gangdese belt, Tibet. *Ore Geol. Rev.* **2019**, *115*, 103169. [CrossRef]
44. Wu, F.Y.; Ji, W.Q.; Liu, C.Z.; Chung, S.L. Detrital zircon U–Pb and Hf isotopic data from the Xigaze fore-arc basin: Constraints on Transhimalayan magmatic evolution in southern Tibet. *Chem. Geol.* **2010**, *271*, 13–25. [CrossRef]
45. Chu, M.F.; Chung, S.L.; Song, B.; Liu, D.Y.; O'Reilly, S.Y.; Pearson, N.J.; Ji, J.Q.; Wen, D.J. Zircon U–Pb and Hf isotope constraints on the Mesozoic tectonics and crustal evolution of Southern Tibet. *Geology* **2006**, *34*, 745–748. [CrossRef]
46. Wen, D.R.; Chung, S.L.; Song, B.; Lizuka, Y.; Yang, H.J.; Ji, J.Q.; Gallet, S. Late Cretaceous Gangdese intrusions of adakitic geochemical characteristics, SE Tibet: Petrogenesis and tectonic implications. *Lithos* **2008**, *105*, 1–11. [CrossRef]
47. Ji, W.Q.; Wu, F.Y.; Liu, C.Z.; Chung, S.L. Early Eocene crustal thickening in southern Tibet: New age and geochemical constraints from the Gangdese batholith. *J. Asian Earth Sci.* **2012**, *53*, 82–95. [CrossRef]
48. Chappell, B.W.; White, A.J.R. Two contrasting granite types. *Pac. Geol.* **1974**, *8*, 173–174.
49. Debon, F.; LeFort, P.; Sheppard, S.M.; Sonet, J. The four plutonic belts of the Transhimalaya–Himalaya: A chemical, mineralogical, isotopic, and chronological synthesis along a Tibet–Nepal section. *J. Petrol.* **1986**, *27*, 219–250. [CrossRef]
50. Hou, Z.Q.; Yang, Z.M.; Qu, X.M.; Meng, X.J.; Li, Z.Q.; Beaudoin, G.; Rui, Z.Y.; Gao, Y.F.; Zaw, K. The Miocene Gangdese porphyry copper belt generated during postcollisional extension in the Tibetan Orogen. *Ore Geol. Rev.* **2009**, *36*, 25–51. [CrossRef]
51. Zheng, Y.Y.; Sun, X.; Gao, S.B. Porphyry mineralization in the Gangdese Orogenic Belt. *Acta Geol. Sin. Engl. Ed.* **2014**, *88*, 662–664. [CrossRef]
52. Lang, X.H.; Deng, Y.L.; Wang, X.H.; Tang, J.X.; Xie, F.W.; Yang, Z.Y.; Jiang, K. Reduced fluids in porphyry copper-gold systems reflect the occurrence of the wall-rock thermogenic process: An example from the No. 1 deposit in the Xiongcun district, Tibet, China. *Ore Geol. Rev.* **2019**, *118*, 103212. [CrossRef]
53. Tang, J.X.; Lang, X.H.; Xie, F.W.; Gao, Y.M.; Li, Z.J.; Huang, Y.; Zhou, Y. Geological characteristics and genesis of the Jurassic No. I porphyry Cu–Au deposit in the Xiongcun district, Gangdese porphyry copper belt, Tibet. *Ore Geol. Rev.* **2015**, *70*, 438–456. [CrossRef]
54. Zhao, J.X.; Qin, K.Z.; Li, G.M.; Li, J.X.; Xiao, B.; Chen, L.; Liu, Y.S. Collision-related genesis of the Sharang porphyry molybdenum deposit, Tibet: Evidence from zircon U–Pb ages, Re–Os ages and Lu–Hf isotopes. *Ore Geol. Rev.* **2014**, *56*, 312–326. [CrossRef]
55. Sun, X.; Hollings, P.; Lu, Y.J. Geology and origin of the Zhunuo porphyry copper deposit, Gangdese belt, southern Tibet. *Mineral. Depos.* **2021**, *56*, 457–480. [CrossRef]
56. Zhao, J.X.; Qin, K.Z.; Xiao, B.; Mclnnes, B.; Li, G.M.; Evans, N.; Li, J.X. Thermal history of the giant Qulong Cu–Mo deposit, Gangdese metallogenic belt, Tibet: Constraints on magmatic–hydrothermal evolution and exhumation. *Gondwana Res.* **2016**, *36*, 390–409. [CrossRef]
57. Zheng, W.B.; Tang, J.X.; Zhong, K.H.; Ying, L.J.; Leng, Q.F.; Ding, S.; Lin, B. Geology of the Jiama porphyry copper-polymetallic system, Lhasa region, China. *Ore Geol. Rev.* **2016**, *74*, 151–169. [CrossRef]
58. Zhou, A.R.G.L.; Dai, J.G.; Li, Y.L.; Li, H.A.; Tang, J.X.; Wang, C.S. Differential exhumation histories between Qulong and Xiongcun porphyry copper deposits in the Gangdese copper metallogenic Belt: Insights from low temperature thermochronology. *Ore Geol. Rev.* **2019**, *107*, 801–819. [CrossRef]
59. Wang, L.Q.; Tang, J.X.; Bagas, L.; Wang, Y.; Lin, X.; Li, Z.; Li, Y.B. Early Eocene Longmala skarn Pb-Zn-Cu deposit in Tibet, China: Geochemistry, fluid inclusions, and H-O-S-Pb isotopic compositions. *Ore Geol. Rev.* **2017**, *88*, 99–115. [CrossRef]
60. Ma, W.; Liu, Y.C.; Yang, Z.S.; Huizenga, J.M.; Li, Z.Q.; Zhao, M.; Yue, L.L.; Zhao, S.B. Petrogenesis of the quartz diorite from the Lietinggang-Leqingla Pb-Zn-Fe-Cu-(Mo) deposit in southern Tibet: Implications for the genesis of a skarn-type polymetallic deposit in the Tibetan-Himalayan collisional orogen. *Ore Geol. Rev.* **2022**, *145*, 104920. [CrossRef]
61. Zheng, Y.C.; Fu, Q.; Hou, Z.Q.; Yang, Z.S.; Huang, K.X.; Wu, C.D.; Sun, Q.Z. Metallogeny of the northeastern Gangdese Pb-Zn-Ag-Fe-Mo-W polymetallic belt in the Lhasa terrane, southern Tibet. *Ore Geol. Rev.* **2015**, *70*, 510–532. [CrossRef]
62. Liu, Y.S.; Hu, Z.C.; Zong, K.Q.; Gao, C.G.; Gao, S.; Xu, J.; Chen, H.H. Reappraisement and refinement of zircon U-Pb isotope and trace element analyses by LA-ICP-MS. *Chin. Sci. Bull.* **2010**, *55*, 1535–1546. [CrossRef]

63. Zhai, D.G.; Liu, J.J.; Zhang, H.Y.; Yao, M.J.; Wang, J.P.; Yang, Y.Q. S-Pb isotopic geochemistry, U-Pb and Re-Os geochronology of the Huanggangling Fe-Sn deposit, Inner Mongolia, NE China. *Ore Geol. Rev.* **2014**, *59*, 109–122. [CrossRef]
64. Qu, X.M.; Wang, R.J.; Xin, H.B.; Zhao, Y.Y.; Fan, X.T. Geochronology and geochemistry of igneous rocks related to the subduction of the Tethys oceanic plate along the Bangong Lake arc zone, the western Tibetan Plateau. *Geochimica* **2009**, *38*, 523–535. (In Chinese with English Abstract)
65. Wang, Y.; Tang, J.X.; Wang, L.Q.; Huizenga, J.M.; Santosh, M.; Zheng, S.L.; Gao, T. Geology, geochronology and geochemistry of the Miocene Jiaoxi quartz vein-type W deposit in the western part of the Lhasa Terrane, Tibet: Implications for ore genesis. *Ore Geol. Rev.* **2020**, *120*, 103433. [CrossRef]
66. Wang, Y.; Tang, J.X.; Wang, L.Q.; Li, S.; Danzhen, W.X.; Li, Z.; Gao, T. Magmatism and metallogenic mechanism of the Ga'erqiong and Galale Cu-Au deposits in the west central Lhasa subterrane, Tibet: Constraints from geochronology, geochemistry, and Sr-Nd-Pb-Hf isotopes. *Ore Geol. Rev.* **2019**, *105*, 616–635. [CrossRef]
67. Corfu, F.; Hanchar, J.M.; Hoskin, P.W.; Kinny, P. Atlas of zircon textures. *Rev. Mineral. Geochem.* **2003**, *53*, 469–495. [CrossRef]
68. Hoskin, P.W.O.; Schaltegger, U. The composition of zircon and igneous and metamorphic petrogenesis. *Rev. Mineral. Geochem.* **2003**, *53*, 27–62. [CrossRef]
69. Rickwood, P.C. Boundary lines within petrologic diagrams which use oxides of major and minor elements. *Lithos* **1989**, *22*, 247–263. [CrossRef]
70. Maniar, P.D.; Piccoli, P.M. Tectonic discrimination of granitoids. *Geol. Soc. Am. Bull.* **1989**, *101*, 635–643. [CrossRef]
71. Ding, S.; Chen, Y.C.; Tang, J.X.; Xie, F.W.; Hu, G.Y.; Yang, Z.Y.; Shi, S.; Li, Y.H.; Yang, H.Y. Relationship between Linzizong volcanic rocks and mineralization: A case study of Sinongduo epithermal Ag-Pb-Zn deposit. *Miner. Depos.* **2017**, *36*, 1074–1092. (In Chinese with English Abstract)
72. Yang, Z.Y.; Tang, J.X.; Santosh, M.; Zhao, X.Y.; Lang, X.H.; Wang, Y.; Ding, S.; Ran, F.Q. Microcontinent subduction and S-type volcanism prior to India-Asia collision. *Sci. Rep.* **2021**, *11*, 14882. [CrossRef] [PubMed]
73. Sun, S.S.; McDonough, W.F. Chemical and isotopic systematics of oceanic basalts: Implications for mantle composition and processes. *Geol. Soc. Lond. Spec. Publ.* **1989**, *42*, 313–345. [CrossRef]
74. Taylor, S.R.; McLennan, S.M. The continental crust: Its composition and evolution. Blackwell Publishing: Oxford, UK, 1985; pp. 301–312.
75. Jackson, M.G.; Hart, S.R.; Koppers, A.A.P.; Staudigel, H.; Konter, J.; Blusztajn, J.; Kurz, M.; Russell, J.A. Te return of subducted continental crust in Samoan lavas. *Nature* **2007**, *448*, 684–687. [CrossRef] [PubMed]
76. McCulloch, M.T.; Arculus, R.J.; Chappell, B.W.; Ferguson, J. Isotopic and geochemical studies of nodules in kimberlite have implications for the lower continental crust. *Nature* **1982**, *300*, 166–169. [CrossRef]
77. Rehkämper, M.; Hofmann, A.W. Recycled ocean crust and sediment in Indian Ocean MORB. *Earth Planet. Sci. Lett.* **1997**, *147*, 93–106. [CrossRef]
78. Plank, T.; Langmuir, C.H. Te chemical composition of subducting sediment and its consequences for the crust and mantle. *Chem. Geol.* **1998**, *145*, 325–394. [CrossRef]
79. Shi, S.; Ding, S.; Yang, Z.Y.; Zou, B. Zircon U-Pb dating of the Miocene granite porphyry in the Sinongduo Ag polymetallic ore deposit in Xietongmen, Tibet, China. *Geol. Rev.* **2017**, *63*, 209–210, (In Chinese with English Abstract).
80. Eby, G.N. Chemical subdivision of the A-type granitoids: Petrogenetic and tectonic implications. *Geology* **1992**, *20*, 641–644. [CrossRef]
81. Chappell, B.W.; White, A.J.R. I-type and S-type granites in the Lachlan fold belt. *Trans. R. Soc. Edinb. Earth Sci.* **1992**, *83*, 1–26.
82. Le Maitre, R.W. Te chemical variability of some common igneous rocks. *J. Pet.* **1976**, *17*, 589–598. [CrossRef]
83. Chappell, B.W.; White, A.J.R. Two contrasting granite types: 25 years later. *Aust. J. Earth Sci.* **2001**, *48*, 489–499. [CrossRef]
84. Bienvenu, P.; Bougault, H.; Joron, J.L.; Treuil, M.; Dmitriev, L. MORB alteration: Rare-earth element/non-rare-earth hygromagmaphile element fractionation. *Chem. Geol.* **1990**, *82*, 1–14. [CrossRef]
85. Lee, C.T.A.; Morton, D.M. High silica granites: Terminal porosity and crystal settling in shallow magma chambers. *Earth Planet. Sci. Lett.* **2015**, *409*, 23–31. [CrossRef]
86. Chappell, B.W.; Bryant, C.J.; Wyborn, D. Peraluminous I-type granites. *Lithos* **2012**, *153*, 142–153. [CrossRef]
87. Yan, H.Y.; Long, X.P.; Li, J.; Wang, Q.; Zhao, B.S.; Shu, C.T.; Gou, L.L.; Zuo, R. Arc andesitic rocks derived from partial melts of Mélange diapir in subduction zones: Evidence from whole-rock geochemistry and Sr–Nd–Mo isotopes of the Paleogene Linzizong volcanic succession in Southern Tibet. *JGR Solid Earth* **2019**, *124*, 456–475. [CrossRef]
88. Ballouard, C.; Poujol, M.; Boulvais, P.; Branquet, Y.; Tartèse, R.; Vigneresse, J.L. Nb–Ta fractionation in peraluminous granites: A marker of the magmatic-hydrothermal transition. *Geology* **2016**, *44*, 231–234. [CrossRef]
89. Taylor, S.R.; McLennan, S.M. The geochemical evolution of the continental crust. *Rev. Geophys.* **1995**, *33*, 241–265. [CrossRef]
90. Zhu, Z.; Campbell, I.H.; Allen, C.M.; Burnham, A.D. S-type granites: Teir origin and distribution through time as determined from detrital zircons. *Earth Planet. Sci. Lett.* **2020**, *536*, 116140.
91. Collins, W.J.; Richards, S.W. Geodynamic signifcance of S-type granites in circum-Pacifc orogens. *Geology* **2008**, *36*, 559–562.
92. Zhou, J.S.; Yang, Z.S.; Wang, Q.; Zheng, Y.C.; Hou, Z.Q.; Wyman, D.A. Extraction of high-silica granites from an upper crustal magma reservoir: Insights from the Narusongduo magmatic system, Gangdese arc. *Am. Miner.* **2020**, *105*, 1572–1584. [CrossRef]
93. Barbarin, B. A review of the relationships between granitoid types, their origins and their geodynamic environments. *Lithos* **1999**, *46*, 605–626. [CrossRef]

94. Sylvester, P.J. Post-collisional strongly peraluminous granites. *Lithos* **1998**, *45*, 29–44. [CrossRef]
95. Hu, X.M.; Garzanti, J.W.; Huang, W.T.; Wei, A.; An, W. The timing of India–Asia collision onset-Facts, theories, controversies. *Earth-Sci. Rev.* **2016**, *160*, 264–299. [CrossRef]
96. Hu, X.; Garzanti, E.; Moore, T.; Raf, I. Direct stratigraphic dating of India–Asia collision onset at the Selandian (middle Paleocene, 59 ± 1 Ma). *Geology* **2015**, *43*, 859–862. [CrossRef]

Disclaimer/Publisher's Note: The statements, opinions and data contained in all publications are solely those of the individual author(s) and contributor(s) and not of MDPI and/or the editor(s). MDPI and/or the editor(s) disclaim responsibility for any injury to people or property resulting from any ideas, methods, instructions or products referred to in the content.